

MODELING, SIMULATION, AND OPTIMIZATION OF SURFACE ACOUSTIC WAVE DRIVEN MICROFLUIDIC BIOCHIPS*

Harbir Antil Roland Glowinski

Department of Mathematics, University of Houston, Houston TX 77204-3008, USA

Email: harbir@math.uh.edu roland@math.uh.edu

Ronald H.W. Hoppe

*Department of Mathematics, University of Houston, Houston TX 77204-3008, USA
and Institute of Mathematics, University of Augsburg, D-86159 Augsburg, Germany*

Email: rohop@math.uh.edu

Christopher Linsenmann

Institute of Mathematics, University of Augsburg, D-86159 Augsburg, Germany

Email: christopher.linsenmann@math.uni-augsburg.de

Tsorng-Whay Pan

Department of Mathematics, University of Houston, Houston TX 77204-3008, USA

Email: pan@math.uh.edu

Achim Wixforth

Institute of Physics, University of Augsburg, D-86159 Augsburg, Germany

Email: achim.wixforth@physik.uni-augsburg.de

Abstract

We will be concerned with the mathematical modeling, numerical simulation, and shape optimization of microfluidic biochips that are used for various biomedical applications. A particular feature is that the fluid flow in the fluidic network on top of the biochips is induced by surface acoustic waves generated by interdigital transducers. We are thus faced with a multiphysics problem that will be modeled by coupling the equations of piezoelectricity with the compressible Navier-Stokes equations. Moreover, the fluid flow exhibits a multiscale character that will be taken care of by a homogenization approach. We will discuss and analyze the mathematical models and deal with their numerical solution by space-time discretizations featuring appropriate finite element approximations with respect to hierarchies of simplicial triangulations of the underlying computational domains. Simulation results will be given for the propagation of the surface acoustic waves on top of the piezoelectric substrate and for the induced fluid flow in the microchannels of the fluidic network. The performance of the operational behavior of the biochips can be significantly improved by shape optimization. In particular, for such purposes we present a multilevel interior point method relying on a predictor-corrector strategy with an adaptive choice of the continuation steplength along the barrier path. As a specific example, we will consider the shape optimization of pressure driven capillary barriers between microchannels and reservoirs.

Mathematics subject classification: 49K20, 49M37, 65K10, 65M60, 65N30, 76N10, 76Z05, 78A70, 90C30, 92C35.

Key words: microfluidic biochips, mathematical modeling, numerical simulation, shape optimization, multiphysics, multiscale problems.

* Received February 6, 2009 / Revised version received May 20, 2009 / Accepted June 6, 2009 /
Published online December 21, 2009 /

1. Introduction

Microfluidic biochips are used in pharmaceutical, medical, and forensic applications for high throughput screening, genotyping, and sequencing in genomics, protein profiling in proteomics, and cytometry in cell analysis [19, 43, 46, 51]. They provide a much better sensitivity and a greater flexibility than traditional approaches and, most importantly, give rise to a significant speed-up of the hybridization processes. This can be achieved by integrating the fluidics on top the chip by means of a lithographically produced network of channels and reservoirs (cf. Fig. 1.1 (left)).

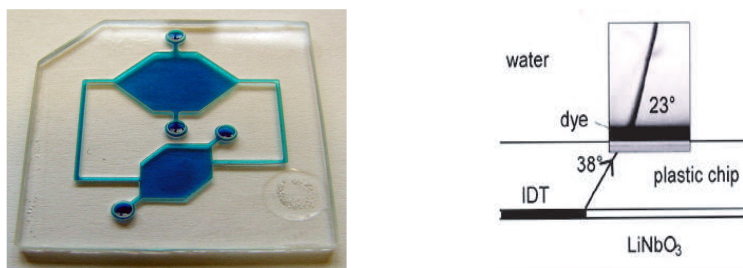


Fig. 1.1. Microfluidic biochip (left) and sharp jet created by surface acoustic waves (right)

The idea is to inject a DNA or protein containing probe and to transport it in the fluid to a reservoir where a chemical analysis is performed. The fluid flow can be taken care of by external pumps which, however, are subject to wear. Instead, a new generation of biochips is based on a surface acoustic waves (SAW) driven fluid flow [25, 53, 54]. Surface acoustic waves are generated by interdigital transducers (IDT), propagate through the base of the device with amplitudes in the range of nanometers and enter the fluid filled microchannels thus creating a sharp jet (cf. Fig. 1.1 (right)). This happens within nanoseconds. The SAWs experience a significant damping along the microchannels which results in a stationary flow pattern, called acoustic streaming. This relaxation process occurs on a time-scale of milliseconds. We are thus faced with a multiscale, multiphysics problem whose mathematical modeling and numerical simulation represents a significant challenge. It is also a challenging problem with regard to various optimization issues such as the optimal design of the microchannels in order to achieve a maximum pumping rate. Another one is the design of pressure driven capillary barriers between the channels and the reservoirs to guarantee a precise filling of the reservoirs with the probes (cf. Fig. 1.2). This amounts to the solution of a shape optimization problem where the mathematical model for the acoustic streaming represents the associated state equations.

The paper is organized as follows: In section 2, we will present a mathematical model for



Fig. 1.2. Capillary barriers

the acoustic streaming that can be derived by a homogenization approach based on the coupling of the equations of piezoelectricity and the compressible Navier-Stokes equations. In section 3, we will discuss numerical methods that have been used for the simulation of the operational behavior of the microfluidic biochips and present simulation results. Section 4 is devoted to the shape optimization of the microchannels by means of a so-called all-at-once approach featuring the simultaneous optimization and numerical solution of the state equations. In particular, we use a primal barrier method in terms of a path-following predictor-corrector continuation scheme with an adaptive choice of the continuation steplength along the barrier path. The barrier method is realized within a multilevel framework using a nested iteration type predictor and a Newton multigrid technique as a corrector. As an application, we consider the shape optimization of pressure driven capillary barriers between microchannels and reservoirs serving as valves for the fluid (cf. Fig. 1.2).

2. Mathematical modeling

In this section, we will develop and analyze a mathematical model describing the operational behavior of SAW driven microfluidic biochips. The model consists of the equations of piezoelectricity unilaterally coupled with the compressible Navier-Stokes equations. In particular, in subsection 2.1 we will be concerned with the piezoelectric equations, whereas subsection 2.2 will be devoted to the compressible Navier-Stokes equations. Using techniques from heterogeneous multiscale methods [14,15], we will derive a compressible Stokes system which serves as a model for the acoustic streaming.

Throughout this section, we will use standard notation from Lebesgue and Sobolev space theory. In particular, for a bounded polygonal or polyhedral domain $\Omega \subset \mathbb{R}^d$, $d \in \{2, 3\}$, with boundary $\Gamma = \partial\Omega$, we denote by $L^2(\Omega)$ and $\mathbf{L}^2(\Omega)$ the Hilbert spaces of scalar and vector-valued Lebesgue integrable functions on Ω with inner products $(\cdot, \cdot)_{0,\Omega}$ and norms $\|\cdot\|_{0,\Omega}$. Likewise, $H^1(\Omega)$ and $\mathbf{H}^1(\Omega)$ refer to the Sobolev spaces with inner products $(\cdot, \cdot)_{1,\Omega}$ and norms $\|\cdot\|_{1,\Omega}$, whereas $H^{1/2}(\Gamma')$ and $\mathbf{H}^{1/2}(\Gamma')$, $\Gamma' \subset \Gamma$, stand for the associated trace spaces. We further refer to $H^{-1}(\Omega)$ and $\mathbf{H}^{-1}(\Omega)$ as the dual spaces of $H_0^1(\Omega)$ and $\mathbf{H}_0^1(\Omega)$, respectively.

2.1. The piezoelectric equations

In piezoelectric materials, the stress tensor $\boldsymbol{\sigma}$ depends linearly on the electric field \mathbf{E} according to a generalized Hooke's law

$$\boldsymbol{\sigma}(\mathbf{u}, \mathbf{E}) = \mathbf{c} \boldsymbol{\varepsilon}(\mathbf{u}) - \mathbf{e} \mathbf{E}. \quad (2.1)$$

Here, $\boldsymbol{\varepsilon}(\mathbf{u}) := (\nabla \mathbf{u} + (\nabla \mathbf{u})^T)/2$ refers to the linearized strain tensor with \mathbf{u} denoting the mechanical displacement, whereas \mathbf{c} and \mathbf{e} stand for the symmetric fourth order elasticity tensor and the symmetric third order piezoelectric tensor, respectively. Hence, the application of an electric field will cause a displacement of the material. Piezoelectric materials also show the reverse effect to generate an electric field when subjected to mechanical stress. These properties are called the piezoelectric effect and the inverse piezoelectric effect. The origin of the piezoelectric effect is related to an asymmetry in the unit cell of a piezoelectric crystal and can be observed only in materials with a polar axis (cf., e.g., [17,37]).

The frequency of the electromagnetic wave is small compared to the frequency of the generated acoustic wave so that a coupling will be neglected. In particular, the electric field will

be considered as quasistatic. Moreover, it is irrotational and hence, according to $\mathbf{E} = -\nabla\Phi$ it can be expressed as the gradient of an electric potential Φ . Since piezoelectric materials are nearly perfect insulators, the only remaining quantity of interest in Maxwell's equations is the dielectric displacement \mathbf{D} which is related to the electric field by the constitutive equation

$$\mathbf{D} = \boldsymbol{\epsilon} \mathbf{E} + \mathbf{P} , \quad (2.2)$$

where $\boldsymbol{\epsilon}$ is the electric permittivity of the material and \mathbf{P} stands for the polarization. In piezoelectric materials, the polarization \mathbf{P} due to external strain is linear, i.e., there holds

$$\mathbf{P} = \mathbf{e} \boldsymbol{\varepsilon}(\mathbf{u}) . \quad (2.3)$$

We assume that the piezoelectric material with density $\rho_p > 0$ occupies some rectangular domain Ω_1 with boundary $\Gamma_1 = \partial\Omega_1$ and exterior unit normal \mathbf{n}_1 such that

$$\begin{aligned} \Gamma_1 &= \bar{\Gamma}_{E,D} \cup \bar{\Gamma}_{E,N}, & \Gamma_{E,D} \cap \Gamma_{E,N} &= \emptyset, \\ \Gamma_1 &= \bar{\Gamma}_{p,D} \cup \bar{\Gamma}_{p,N}, & \Gamma_{p,D} \cap \Gamma_{p,N} &= \emptyset, \end{aligned}$$

where $\Gamma_{E,D}$ is a rectangular subdomain of the upper boundary of Γ_1 and $\Gamma_{E,N} := \Gamma_1 \setminus \bar{\Gamma}_{E,D}$. Given boundary data $\Phi_{E,D}$ on $\Gamma_{E,D}$, the pair (\mathbf{u}, Φ) satisfies the following initial-boundary value problem for the piezoelectric equations

$$\rho_p \frac{\partial^2 \mathbf{u}}{\partial t^2} - \nabla \cdot \boldsymbol{\sigma}(\mathbf{u}, \mathbf{E}) = 0 \quad \text{in } Q_1 := \Omega_1 \times (0, T_1), \quad (2.4a)$$

$$\nabla \cdot \mathbf{D}(\mathbf{u}, \mathbf{E}) = 0 \quad \text{in } Q_1, \quad (2.4b)$$

$$\mathbf{u} = 0 \quad \text{on } \Gamma_{p,D}, \quad \mathbf{n}_1 \cdot \boldsymbol{\sigma} = \boldsymbol{\sigma}_{\mathbf{n}_1} \quad \text{on } \Gamma_{p,N}, \quad (2.4c)$$

$$\Phi = \Phi_{E,D} \quad \text{on } \Gamma_{E,D}, \quad \mathbf{n}_1 \cdot \mathbf{D} = D_{\mathbf{n}_1} \quad \text{on } \Gamma_{E,N}, \quad (2.4d)$$

$$\mathbf{u}(\cdot, 0) = 0, \quad \frac{\partial \mathbf{u}}{\partial t}(\cdot, 0) = 0 \quad \text{in } \Omega_1, \quad (2.4e)$$

which have to be completed by the constitutive equations (2.1)-(2.3).

Assuming time periodic excitations

$$\Phi_{E,D}(\cdot, t) = \text{Re} \left(\hat{\Phi}_{E,D} \exp(-i\omega t) \right)$$

such that $\hat{\Phi}_{E,D} \in H^{1/2}(\Gamma_{E,D})$, we are looking for time harmonic solutions

$$\mathbf{u}(\cdot, t) = \text{Re} (\mathbf{u}(\cdot) \exp(-i\omega t)), \quad \Phi(\cdot, t) = \text{Re} (\Phi(\cdot) \exp(-i\omega t)).$$

This leads to a saddle point problem for a Helmholtz-type equation which in its weak form amounts to the computation of $(\mathbf{u}, \Phi) \in \mathbf{V} \times W$, where

$$\mathbf{V}_0 := H_{0,\Gamma_{p,D}}^1(\Omega_1)^3 \text{ and } W := \left\{ \varphi \in H^1(\Omega_1) \mid \varphi_{\Gamma_{E,D}} = \hat{\Phi}_{E,D} \right\},$$

such that for all $\mathbf{v} \in \mathbf{V}$ and $\psi \in W_0 := H_{0,\Gamma_{E,D}}^1(\Omega_1)$

$$a(\mathbf{u}, \mathbf{v}) + b(\Phi, \mathbf{v}) - \omega^2 \rho_p (\mathbf{u}, \mathbf{v})_{0,\Omega} = \ell_1(\mathbf{v}), \quad (2.5a)$$

$$b(\psi, \mathbf{u}) - c(\Phi, \psi) = \ell_2(\psi). \quad (2.5b)$$

Here,

$$H_{0,\Gamma_{p,D}}^1(\Omega_1)^3 := \left\{ \mathbf{v} \in H^1(\Omega_1)^3 \mid \mathbf{v}|_{\Gamma_{p,D}} = 0 \right\},$$

$$H_{0,\Gamma_{E,D}}^1(\Omega_1) := \left\{ \psi \in H^1(\Omega_1) \mid \psi|_{\Gamma_{E,D}} = 0 \right\},$$

and the sesquilinear forms $a(\cdot, \cdot)$, $b(\cdot, \cdot)$, $c(\cdot, \cdot)$ and the functionals $\ell_1 \in \mathbf{V}^*$, $\ell_2 \in W^*$ are given by

$$a(\mathbf{v}, \mathbf{w}) := \int_{\Omega_1} \mathbf{c} \boldsymbol{\varepsilon}(\mathbf{v}) : \boldsymbol{\varepsilon}(\bar{\mathbf{w}}) \, dx, \quad b(\varphi, \mathbf{v}) := \int_{\Omega_1} \boldsymbol{\varepsilon} \nabla \varphi : \boldsymbol{\varepsilon}(\bar{\mathbf{v}}) \, dx,$$

$$c(\varphi, \psi) := \int_{\Omega_1} \boldsymbol{\varepsilon} \nabla \varphi \cdot \nabla \bar{\psi} \, dx,$$

$$\ell_1(\mathbf{v}) := \langle \boldsymbol{\sigma}_{\mathbf{n}_1}, \mathbf{v} \rangle_{p,N}, \quad \ell_2(\psi) := \langle D_{\mathbf{n}_1}, \psi \rangle_{E,N},$$

with $\langle \cdot, \cdot \rangle_{p,N}$, $\langle \cdot, \cdot \rangle_{E,N}$ denoting the dual pairings between the associated trace spaces and their dual spaces, respectively.

We denote by $\mathbf{A} : \mathbf{V} \rightarrow \mathbf{V}^*$, $\mathbf{B} : W \rightarrow \mathbf{V}^*$, and $\mathbf{C} : W \rightarrow W^*$ the operators associated with the sesquilinear forms and by \mathbf{I} the injection $\mathbf{I} : \mathbf{V} \rightarrow \mathbf{V}^*$. Then, an equivalent formulation of (2.5) is

$$(\mathbf{A} - \omega^2 \rho_p \mathbf{I})\mathbf{u} + \mathbf{B}\Phi = \mathbf{f}, \quad (2.6a)$$

$$\mathbf{B}^*\mathbf{u} - \mathbf{C}\Phi = f. \quad (2.6b)$$

Here, the right-hand sides $\mathbf{f} \in \mathbf{V}^*$ and $f \in W^*$ are given by

$$\mathbf{f} := \ell_1 - \mathbf{B}\tilde{\Phi}_{E,D}, \quad f := \ell_2 + \mathbf{C}\tilde{\Phi}_{E,D}, \quad (2.7)$$

where $\tilde{\Phi}_{E,D}$ stands for the extension of the Dirichlet data onto W .

In particular, the operator \mathbf{A} is symmetric and \mathbf{V} -elliptic, and the operator \mathbf{C} is symmetric and W -elliptic. The symmetry of \mathbf{A} results from the symmetry of the elasticity tensor \mathbf{c} , whereas the \mathbf{V} -ellipticity is a direct consequence of the positive definiteness of \mathbf{c} and Korn's inequality. Likewise, the symmetry of \mathbf{C} follows from the symmetry of the dielectric permittivity $\boldsymbol{\varepsilon}$ and the W -ellipticity can be deduced from the positive definiteness of $\boldsymbol{\varepsilon}$.

Elimination of Φ from (2.6) results in the Schur complement system

$$\mathbf{S}\mathbf{u} - \omega^2 \rho_p \mathbf{u} = \mathbf{g}. \quad (2.8)$$

Here, the Schur complement operator $\mathbf{S} : \mathbf{V} \rightarrow \mathbf{V}^*$ is defined according to

$$\mathbf{S} := \mathbf{A} + \mathbf{B}\mathbf{C}^{-1}\mathbf{B}^*, \quad (2.9)$$

whereas the right-hand side \mathbf{g} is given by

$$\mathbf{g} := \mathbf{f} + \mathbf{B}\mathbf{C}^{-1}f. \quad (2.10)$$

Theorem 2.1. *For the Schur complement \mathbf{S} given by (2.9) and the Schur complement system (2.8) there holds:*

- (i) *The spectrum of \mathbf{S} consists of a sequence of countably many real eigenvalues $0 < \zeta_1^2 < \zeta_2^2 < \dots$ tending to infinity, i.e., $\lim_{j \rightarrow \infty} \zeta_j^2 = \infty$.*

(ii) If $\omega^2 \rho_p$ is not an eigenvalue of \mathbf{S} , for every $\mathbf{g} \in \mathbf{V}^*$, (2.8) admits a unique solution $\mathbf{u} \in \mathbf{V}$ depending continuously on \mathbf{g} .

(iii) If $\omega^2 \rho_p \in \mathbb{R}$ is an eigenvalue of \mathbf{S} , (2.8) is solvable if and only if $\mathbf{g} \in \text{Ker}(\mathbf{S} - \omega^2 \rho_p \mathbf{I})^0$ where

$$\text{Ker}(\mathbf{S} - \omega^2 \rho_p \mathbf{I})^0 := \left\{ \mathbf{v}^* \in \mathbf{V}^* \mid \langle \mathbf{v}^*, \mathbf{v} \rangle = 0, \mathbf{v} \in \text{Ker}(\mathbf{S} - \omega^2 \rho_p \mathbf{I}) \right\}.$$

Proof. The Schur complement system (2.8) can be rewritten according to

$$\mathbf{S} \mathbf{u} - \omega^2 \rho_p \mathbf{u} = -\omega^2 \rho_p \mathbf{S} \left(\mathbf{S}_R^{-1} - \omega^{-2} \rho_p^{-1} \mathbf{I} \right) \mathbf{u} = \mathbf{g},$$

where $\mathbf{S}_R^{-1} : \mathbf{L}^2(\Omega_1) \rightarrow \mathbf{V}$ is given by $\mathbf{S}_R^{-1} \mathbf{v} = \mathbf{S}^{-1} \mathbf{v}$, $\mathbf{v} \in \mathbf{L}^2(\Omega_1)$. It is easy to see that \mathbf{S}_R^{-1} is a compact self-adjoint endomorphism on $\mathbf{L}^2(\Omega_1)$ and hence, the assertions (i), (ii), and (iii) follow from the Hilbert-Schmidt theory and the Fredholm alternative (cf., e.g., [55]). \square

2.2. The compressible Navier-Stokes equations

Since compressible effects dominate the SAW induced fluid flow, it has to be described by the compressible Navier-Stokes equations. We denote by $\Omega_2(t), t \in [0, T_2]$, the time dependent domain occupied by the fluid with boundary $\Gamma_2(t) = \overline{\Gamma(t)}_{2,D} \cup \overline{\Gamma(t)}_{2,N}$, $\Gamma_{2,D}(t) \cap \Gamma_{2,N}(t) = \emptyset$. Here, $\Gamma_{2,D}(t)$ is that part of the boundary where the SAWs enter the fluid filled microchannels. We assume that the coupling between the piezoelectric and the Navier-Stokes equations is unilateral and occurs by means of the deflection of the walls of the microchannels caused by the SAWs. We denote by \mathbf{v} and p the velocity and the pressure, and we refer to ρ_f, η , and ξ as the density of the fluid and the standard and bulk viscosities. Then, the pair (\mathbf{v}, p) satisfies the following initial-boundary value problem

$$\rho_f \left(\frac{\partial \mathbf{v}}{\partial t} + \mathbf{v} \cdot \nabla \mathbf{v} \right) = \nabla \cdot \boldsymbol{\sigma}, \quad (2.11a)$$

$$\frac{\partial \rho_f}{\partial t} + \nabla \cdot (\rho_f \mathbf{v}) = 0, \quad \text{in } Q_2 := \Omega_2(t) \times (0, T_2), \quad (2.11b)$$

$$\mathbf{v}(\cdot + \mathbf{u}(\cdot, t), t) = \frac{\partial \mathbf{u}}{\partial t}(\cdot, t), \quad \text{on } \Gamma_{2,D}(t), \quad t \in (0, T_2), \quad (2.11c)$$

$$\boldsymbol{\sigma} \mathbf{n} = 0, \quad \text{on } \Gamma_{2,N}(t), \quad t \in (0, T_2), \quad (2.11d)$$

$$\mathbf{v}(\cdot, 0) = \mathbf{v}_0, \quad p(\cdot, 0) = p_0, \quad \text{in } \Omega_2(0), \quad (2.11e)$$

where $\boldsymbol{\sigma} = (\sigma_{ij})_{i,j=1}^d$, $\sigma_{ij} := -p \delta_{ij} + 2\eta \varepsilon_{ij}(\mathbf{v}) + \delta_{ij}(\xi - 2\eta/3) \nabla \cdot \mathbf{v}$ in (2.11d). Since the deflection of the walls of the microchannels by the SAWs is approximately $10^{-9} m$ compared to lengths, widths, and heights of the microchannels in the range of μm to mm , in the sequel we will neglect the time dependence of Ω_2 .

The SAW induced fluid flow exhibits two different time scales. When the SAWs enter the fluid filled microchannels, sharp jets and vortices are created within nanoseconds (cf. Fig. 1.1 (right)). The SAWs propagate along the channels and experience a significant damping which results in a stationary flow pattern, called acoustic streaming. This relaxation process happens on a time scale of milliseconds. The multiscale character can be appropriately taken care of by a homogenization approach. Following [2, 35], we introduce a scale parameter $\varepsilon > 0$

which represents the maximum deflection of the walls of the microchannels, and we consider the asymptotic expansions

$$\begin{aligned}\rho_f &= \rho_{f,0} + \varepsilon \rho'_f + \varepsilon^2 \rho''_f + \mathcal{O}(\varepsilon^3), \\ \mathbf{v} &= \mathbf{v}_0 + \varepsilon \mathbf{v}' + \varepsilon^2 \mathbf{v}'' + \mathcal{O}(\varepsilon^3), \\ p &= p_0 + \varepsilon p' + \varepsilon^2 p'' + \mathcal{O}(\varepsilon^3).\end{aligned}$$

Collecting all terms of order $\mathcal{O}(\varepsilon)$, assuming $\mathbf{v}_0 \equiv 0$ (fluid at rest, if no SAW actuation), and setting $\rho_{f,1} = \varepsilon \rho'_f$, $\mathbf{v}_1 := \varepsilon \mathbf{v}'$, $p_1 := \varepsilon p'$, we find that the triple $(\rho_{f,1}, \mathbf{v}_1, p_1)$ satisfies the linear system

$$\rho_{f,0} \frac{\partial \mathbf{v}_1}{\partial t} - \nabla \cdot \boldsymbol{\sigma}_1 = \mathbf{0} \quad \text{in } Q_2, \quad (2.12a)$$

$$\frac{\partial \rho_{f,1}}{\partial t} + \rho_{f,0} \nabla \cdot \mathbf{v}_1 = 0 \quad \text{in } Q_2, \quad (2.12b)$$

$$\mathbf{v}_1 = \mathbf{g}_1 \quad \text{on } \Gamma_{2,D}, \quad t > 0, \quad (2.12c)$$

$$\boldsymbol{\sigma}_1 \mathbf{n} = 0 \quad \text{on } \Gamma_{2,N}, \quad t > 0, \quad (2.12d)$$

$$\mathbf{v}_1(\cdot, 0) = 0, \quad p_1(\cdot, 0) = 0 \quad \text{in } \Omega_2, \quad (2.12e)$$

where $\boldsymbol{\sigma}_1 = ((\sigma_1)_{ij})_{i,j=1}^d$, $(\sigma_1)_{ij} := -p \delta_{ij} + 2\eta \varepsilon_{ij}(\mathbf{v}_1) + \delta_{ij}(\xi - 2\eta/3)\nabla \cdot \mathbf{v}_1$, $\mathbf{g}_1 := \partial \mathbf{u} / \partial t$ and where p_1 and $\rho_{f,1}$ are related by the constitutive equation

$$p_1 = c_0^2 \rho_{f,1} \quad \text{in } Q_2. \quad (2.13)$$

Here, c_0 stands for the small signal sound speed in the fluid. The system describes the propagation and damping of the acoustic waves in the microchannels.

We substitute $\rho_{f,1}$ in (2.12b) by means of (2.13) and introduce the function spaces

$$\begin{aligned}\mathbf{V}_{\mathbf{g}_1} &:= \left\{ \mathbf{v} \in L^2((0, T); H^1(\Omega_2)^3) \cap H^1((0, T); H^{-1}(\Omega_2)^3) \mid \mathbf{v}|_{\Gamma_{2,D}} = \mathbf{g}_1 \right\}, \\ W_0 &:= H^1\left((0, T); L_0^2(\Omega_2)\right).\end{aligned}$$

The weak formulation of (2.12) amounts to the computation of $(\mathbf{v}_1, p_1) \in \mathbf{V}_{\mathbf{g}_1} \times W_0$ such that for all $(\mathbf{w}, q) \in \mathbf{H}_{0,\Gamma_{2,D}}^1(\Omega_2) \times L_0^2(\Omega_2)$ there holds

$$\left\langle \rho_{f,0} \frac{\partial \mathbf{v}_1}{\partial t}, \mathbf{w} \right\rangle + a(\mathbf{v}_1, \mathbf{w}) + b(p_1, \mathbf{w}) = 0, \quad (2.14a)$$

$$\left(\rho_{f,0}^{-1} c_0^{-2} \frac{\partial p_1}{\partial t}, q \right)_{0,\Omega_2} - b(q, \mathbf{v}_1) = 0, \quad (2.14b)$$

$$\mathbf{v}_1(\cdot, 0) = 0, \quad p_1(\cdot, 0) = 0. \quad (2.14c)$$

Here, $\langle \cdot, \cdot \rangle$ stands for the respective dual pairing, and the bilinear forms $a(\cdot, \cdot)$ and $b(\cdot, \cdot)$ are given by

$$a(\mathbf{v}, \mathbf{w}) := \eta \int_{\Omega_2} \nabla \mathbf{v} : \nabla \mathbf{w} \, dx + \left(\xi + \frac{\eta}{3} \right) \int_{\Omega_2} \nabla \cdot \mathbf{v} \nabla \cdot \mathbf{w} \, dx, \quad (2.15a)$$

$$b(p, \mathbf{w}) := - \int_{\Omega_2} p \nabla \cdot \mathbf{w} \, dx. \quad (2.15b)$$

For time periodic excitations \mathbf{g}_1 , we also consider the time periodic problem: Find $(\mathbf{v}_1, p_1) \in \mathbf{V}_{\mathbf{g}_1} \times W_0$ such that for all $(\mathbf{w}, q) \in \mathbf{H}_{0,\Gamma_{2,D}}^1(\Omega_2) \times L_0^2(\Omega_2)$ there holds

$$\left\langle \rho_{f,0} \frac{\partial \mathbf{v}_1}{\partial t}, \mathbf{w} \right\rangle + a(\mathbf{v}_1, \mathbf{w}) + b(p_1, \mathbf{w}) = 0, \quad (2.16a)$$

$$\left(\rho_{f,0}^{-1} c_0^{-2} \frac{\partial p_1}{\partial t}, q \right)_{0,\Omega_2} - b(q, \mathbf{v}_1) = 0, \quad (2.16b)$$

$$\mathbf{v}_1(\cdot, 0) = \mathbf{v}_1(\cdot, T), \quad p_1(\cdot, 0) = p_1(\cdot, T). \quad (2.16c)$$

Theorem 2.2. *For the solution of the variational problems (2.14) and (2.16) there holds:*

- (i) For $\mathbf{g}_1 \in \mathbf{L}^2((0, T); \mathbf{H}^{1/2}(\Gamma_{2,D}))$ there exists a unique solution $(\mathbf{v}_1, p_1) \in \mathbf{V}_{\mathbf{g}} \times W_0$ of (2.14) satisfying the stability estimate

$$\|(\mathbf{v}_1, p_1)\|_{\mathbf{V}_{\mathbf{g}} \times W_0} \leq C_T \|\mathbf{g}_1\|_{\mathbf{L}^2((0, T); \mathbf{H}^{1/2}(\Gamma_{2,D}))}, \quad (2.17)$$

where $C_T > 0$ is a constant depending on T .

- (ii) If the forcing term \mathbf{g}_1 is time periodic, then there exists a unique solution (\mathbf{v}_1, p_1) of (2.16).

Proof. Taking advantage of the ellipticity of the bilinear form $a(\cdot, \cdot)$, i.e.,

$$a(\mathbf{v}, \mathbf{v}) \geq \alpha \|\mathbf{v}\|_{1,\Omega_2}^2, \quad \alpha > 0,$$

and the fact that the bilinear form $b(\cdot, \cdot)$ satisfies the inf-sup condition

$$\inf_{q \in L_0^2(\Omega_2) \setminus \{0\}} \sup_{\mathbf{v} \in \mathbf{H}_{0,\Gamma_{2,D}}^1(\Omega_2) \setminus \{0\}} \frac{b(q, \mathbf{v})}{\|q\|_{0,\Omega_2} \|\mathbf{v}\|_{1,\Omega_2}} \geq \beta > 0,$$

the existence of a solution $(\mathbf{v}_1, p_1) \in \mathbf{V}_{\mathbf{g}} \times W_0$ of (2.14a)-(2.14c) satisfying (2.17) can be shown by standard arguments based on the Galerkin method (cf., e.g., [44]). The uniqueness is an immediate consequence of (2.17). For the proof of (ii) we refer to Theorem 3.12 in [35]. \square

Collecting all terms of order $\mathcal{O}(\varepsilon^2)$, neglecting time derivatives, and performing the time-averaging $\langle w \rangle := T^{-1} \int_{t_0}^{t_0+T} w dt$, where $T := 2\pi/\omega$, we arrive at the compressible Stokes system

$$-\nabla \cdot \boldsymbol{\sigma}_2 = \left\langle -\rho_{f,1} \frac{\partial \mathbf{v}_1}{\partial t} - \rho_{f,0} [\nabla \mathbf{v}_1] \mathbf{v}_1 \right\rangle \quad \text{in } \Omega_2, \quad (2.18a)$$

$$\rho_{f,0} \nabla \cdot \mathbf{v}_2 = \left\langle -\nabla \cdot (\rho_{f,1} \mathbf{v}_1) \right\rangle \quad \text{in } \Omega_2, \quad (2.18b)$$

$$\mathbf{v}_2 = \mathbf{g}_2 \quad \text{on } \Gamma_{2,D}, \quad (2.18c)$$

$$\boldsymbol{\sigma}_2 \mathbf{n} = 0 \quad \text{on } \Gamma_{2,N} \quad (2.18d)$$

where $\boldsymbol{\sigma}_2 = ((\sigma_2)_{ij})_{i,j=1}^d$, $(\sigma_2)_{ij} := -p \delta_{ij} + 2\eta \varepsilon_{ij}(\mathbf{v}_2) + \delta_{ij}(\xi - 2\eta/3) \nabla \cdot \mathbf{v}_2$, $\mathbf{g}_2 := -\langle [\nabla \mathbf{v}_1] \mathbf{u} \rangle$. The density $\rho_{f,2}$ can be obtained via the constitutive equation

$$p_2 = c_0^2 \rho_{f,2}. \quad (2.19)$$

The compressible Stokes system (2.18a)-(2.18c) is used as a model for the acoustic streaming, i.e., the stationary flow pattern which forms on a time scale of milliseconds.

The weak formulation of (2.18) requires the computation of $(\mathbf{v}_2, p_2) \in \mathbf{V}_{\mathbf{g}_2} \times L_0^2(\Omega_2)$, where

$$\mathbf{V}_{\mathbf{g}_2} := \left\{ \mathbf{v} \in \mathbf{H}^1(\Omega_2) \mid \mathbf{v}|_{\Gamma_{2,N}} = \mathbf{g}_2 \right\},$$

such that

$$a(\mathbf{v}_2, \mathbf{w}) + b(p_2, \mathbf{w}) = (\mathbf{f}, \mathbf{w})_{0,\Omega}, \quad \mathbf{w} \in \mathbf{V}_0, \quad (2.20a)$$

$$b(q, \mathbf{v}_2) = (f, q)_{0,\Omega_2}, \quad q \in L_0^2(\Omega_2). \quad (2.20b)$$

Here, the bilinear forms $a(\cdot, \cdot), b(\cdot, \cdot)$ are as in (2.15a),(2.15b), and the right-hand sides \mathbf{f}, f are given by

$$\mathbf{f} := - \left\langle \rho_{f,1} \frac{\partial \mathbf{v}_1}{\partial t} - \rho_{f,0} [\nabla \mathbf{v}_1] \mathbf{v}_1 \right\rangle, \quad f := \langle \rho_{f,0}^{-1} \nabla \cdot (\rho_{f,1} \mathbf{v}_1) \rangle.$$

Theorem 2.3. *If $\mathbf{f} \in \mathbf{L}^2(\Omega_2), f \in L^2(\Omega_2)$, and $\mathbf{g}_2 \in \mathbf{H}^{1/2}(\Gamma_{2,D})$, then the weak formulation (2.20) of the compressible Stokes system admits a unique solution $(\mathbf{v}_2, p_2) \in \mathbf{V}_{\mathbf{g}_2} \times L_0^2(\Omega_2)$ depending continuously on the data according to*

$$\|(\mathbf{v}_2, p_2)\|_{\mathbf{V}_{\mathbf{g}_2} \times L_0^2(\Omega_2)} \leq C \left(\|\mathbf{f}\|_{0,\Omega_2} + \|f\|_{0,\Omega_2} + \|\mathbf{g}_2\|_{\mathbf{H}^{1/2}(\Gamma_{2,D})} \right), \quad (2.21)$$

where C is a positive constant.

Proof. Due to the ellipticity of $a(\cdot, \cdot)$ and the inf-sup condition satisfied by $b(\cdot, \cdot)$, the proof follows by standard arguments (cf., e.g., [9]). \square

3. Numerical simulation

3.1. Simulation of SAWs

We assume $\mathcal{T}_h(\Omega_1)$ to be a geometrically conforming, simplicial triangulation of the computational domain Ω_1 . We denote by \mathbf{V}_h the finite element space of vector fields with continuous, piecewise linear components, whereas W_h refers to the finite element space of continuous, piecewise linear scalar functions. Then, the finite element approximation of the saddle point problem (2.5a),(2.5b) amounts to the computation of $(\mathbf{u}_h, \Phi_h) \in \mathbf{V}_h \times W_h$ such that for all $(\mathbf{v}_h, \psi_h) \in \mathbf{V}_h \times W_h$ there holds

$$a(\mathbf{u}_h, \mathbf{v}_h) + b(\Phi_h, \mathbf{v}_h) - \omega^2(\mathbf{u}_h, \mathbf{v}_h)_{0,\Omega} = \ell_1(\mathbf{v}_h), \quad (3.1a)$$

$$b(\psi_h, \mathbf{u}_h) - c(\Phi_h, \psi_h) = \ell_2(\psi_h). \quad (3.1b)$$

We denote by $\mathbf{A}_h : \mathbf{V}_h \rightarrow \mathbf{V}_h^*, \mathbf{B}_h : W_h \rightarrow \mathbf{V}_h^*, \mathbf{C}_h : W_h \rightarrow W_h^*$ the operators associated with the restrictions $a|_{\mathbf{V}_h \times \mathbf{V}_h}, b|_{W_h \times \mathbf{V}_h}, c|_{W_h \times W_h}$, and by \mathbf{I}_h the injection $\mathbf{I}_h : \mathbf{V}_h \rightarrow \mathbf{V}_h^*$. We further define $\mathbf{f}_h \in \mathbf{V}_h^*$ and $f \in W_h^*$ by $\langle \mathbf{f}_h, \mathbf{v}_h \rangle := \langle \mathbf{f}, \mathbf{v}_h \rangle, \mathbf{v}_h \in \mathbf{V}_h$, and $\langle f_h, w_h \rangle := \langle f, w_h \rangle, w_h \in W_h$, where $\mathbf{f} \in \mathbf{V}^*$ and $f \in W^*$ are given by (2.7). Then, the operator form of (3.1) reads as follows:

$$(\mathbf{A}_h - \omega^2 \mathbf{I}_h) \mathbf{u}_h + \mathbf{B}_h \Phi_h = \mathbf{f}_h, \quad (3.2a)$$

$$\mathbf{B}_h^* \mathbf{u}_h - \mathbf{C}_h \Phi_h = f_h. \quad (3.2b)$$

Static condensation of the discrete electric potential Φ_h gives rise to the discrete Schur complement system

$$\mathbf{S}_h \mathbf{u}_h - \omega^2 \mathbf{u}_h = \mathbf{g}_h, \quad (3.3)$$

where the discrete Schur complement \mathbf{S}_h and the right-hand side \mathbf{g}_h are given by

$$\mathbf{S}_h := \mathbf{A}_h + \mathbf{B}_h \mathbf{C}_h^{-1} \mathbf{B}_h^*, \quad \mathbf{g}_h := \mathbf{f}_h + \mathbf{B}_h \mathbf{C}_h^{-1} f_h.$$

Theorem 3.1. *Assume that ω^2 is not an eigenvalue of the Schur complement \mathbf{S} as given by (2.9). Then, for sufficiently small h the discrete Schur complement system (3.3) admits a unique solution $\mathbf{u}_h \in \mathbf{V}_h$.*

Proof. If ω^2 is not an eigenvalue of \mathbf{S} , the inf-sup condition

$$\inf_{\mathbf{v} \in \mathbf{V} \setminus \{0\}} \sup_{\mathbf{w} \in \mathbf{V} \setminus \{0\}} \frac{|((\mathbf{S} - \omega^2 \mathbf{I})\mathbf{v}, \mathbf{w})|}{\|\mathbf{v}\|_{1, \Omega_1} \|\mathbf{w}\|_{1, \Omega_1}} \geq \beta > 0$$

holds true which implies

$$\begin{aligned} \beta \|\mathbf{v}\|_{1, \Omega_1} &\leq \sup_{\mathbf{w} \in \mathbf{V} \setminus \{0\}} \frac{|((\mathbf{S} - \omega^2 \mathbf{I})\mathbf{v}, \mathbf{w})|}{\|\mathbf{w}\|_{1, \Omega_1}} \\ &= \sup_{\mathbf{w} \in \mathbf{V} \setminus \{0\}} \frac{|((\mathbf{S}(\mathbf{v} - \omega^2 \mathbf{S}^{-1} \mathbf{v}), \mathbf{w})|}{\|\mathbf{w}\|_{1, \Omega_1}} \leq \|\mathbf{S}\| \|\mathbf{v} - \omega^2 \mathbf{S}^{-1} \mathbf{v}\|_{1, \Omega_1}. \end{aligned} \quad (3.4)$$

On the other hand, we note that \mathbf{S}_h is the Galerkin approximation of \mathbf{S} , i.e.,

$$\langle \mathbf{S}_h \mathbf{v}_h, \mathbf{w}_h \rangle = \langle \mathbf{S} \mathbf{v}_h, \mathbf{w}_h \rangle, \quad \mathbf{v}_h, \mathbf{w}_h \in \mathbf{V}_h.$$

Hence, referring to $\alpha_S > 0$ as the ellipticity constant of \mathbf{S} , we have

$$\langle \mathbf{S}_h \mathbf{v}_h, \mathbf{v}_h \rangle \geq \alpha_S \|\mathbf{v}_h\|_{1, \Omega_1}^2, \quad \mathbf{v}_h \in \mathbf{V}_h. \quad (3.5)$$

Using (3.5), we deduce from (3.4) that

$$\begin{aligned} &\sup_{\mathbf{0} \neq \mathbf{w}_h \in \mathbf{V}_h} \frac{|\langle (\mathbf{S}_h - \omega^2 \mathbf{I}_h) \mathbf{v}_h, \mathbf{w}_h \rangle|}{\|\mathbf{w}_h\|_{1, \Omega_1}} \\ &= \sup_{\mathbf{0} \neq \mathbf{w}_h \in \mathbf{V}_h} \frac{|\langle \mathbf{S}_h (\mathbf{v}_h - \omega^2 \mathbf{S}_h^{-1} \mathbf{v}_h), \mathbf{w}_h \rangle|}{\|\mathbf{w}_h\|_{1, \Omega_1}} \\ &\geq \frac{|\langle \mathbf{S}_h (\mathbf{v}_h - \omega^2 \mathbf{S}_h^{-1} \mathbf{v}_h), \mathbf{v}_h - \omega^2 \mathbf{S}_h^{-1} \mathbf{v}_h \rangle|}{\|\mathbf{v}_h - \omega^2 \mathbf{S}_h^{-1} \mathbf{v}_h\|_{1, \Omega_1}} \geq \alpha_S \|\mathbf{v}_h - \omega^2 \mathbf{S}_h^{-1} \mathbf{v}_h\|_{1, \Omega_1} \\ &\geq \alpha_S \left(\|\mathbf{v}_h - \omega^2 \mathbf{S}^{-1} \mathbf{v}_h\|_{1, \Omega_1} - \omega^2 \|(\mathbf{S}_h^{-1} - \mathbf{S}^{-1}) \mathbf{v}_h\|_{1, \Omega_1} \right) \\ &\geq \beta_h \|\mathbf{v}_h\|_{1, \Omega_1}, \end{aligned}$$

where

$$\beta_h := \alpha_S \left(\frac{\beta}{\|\mathbf{S}\|} - \omega^2 \|\mathbf{S}_h^{-1} - \mathbf{S}^{-1}\| \right).$$

Since $\mathbf{S}_h^{-1} \rightarrow \mathbf{S}^{-1}$ as $h \rightarrow 0$, there exists $h_{max} > 0$ such that $\beta_h \geq \gamma > 0$ uniformly for $h \leq h_{max}$. This shows that $\mathbf{S}_h - \omega^2 \mathbf{I}_h$ asymptotically satisfies a discrete inf-sup condition which gives the assertion. \square

The discrete saddle point problem (3.1) can be written equivalently as the algebraic saddle point problem

$$\begin{pmatrix} A & B \\ B^T & -C \end{pmatrix} \begin{pmatrix} u \\ \Phi \end{pmatrix} = \begin{pmatrix} b_1 \\ b_2 \end{pmatrix}, \quad (3.6)$$

where $A \in \mathbb{R}^{n_h \times n_h}$, $n_h := \dim \mathbf{V}_h$, and $C \in \mathbb{R}^{m_h \times m_h}$, $m_h := \dim W_h$, are symmetric positive definite matrices, $B \in \mathbb{R}^{n_h \times m_h}$, and $b_1 \in \mathbb{R}^{n_h}$, $b_2 \in \mathbb{R}^{m_h}$. We have solved (3.6) by preconditioned GMRES using a block-diagonal preconditioner P of the form

$$P = \begin{pmatrix} \tilde{A} & 0 \\ 0 & \tilde{C} \end{pmatrix}$$

such that

$$\begin{aligned} \gamma_A v^T \tilde{A} v &\leq v^T A v \leq \Gamma_A v^T \tilde{A} v, \\ \gamma_C w^T \tilde{C} w &\leq w^T C w \leq \Gamma_C w^T \tilde{C} w, \end{aligned}$$

with constants $0 < \gamma_A \leq \Gamma_A$, $0 < \gamma_C \leq \Gamma_C$ satisfying $\Gamma_A/\gamma_A \ll \kappa(A)$, $\Gamma_C/\gamma_C \ll \kappa(C)$, where $\kappa(A)$, $\kappa(C)$ are the spectral radii of A and C , respectively. We have realized \tilde{A}^{-1} and \tilde{C}^{-1} by BPX preconditioners with respect to a hierarchy $\{\mathcal{T}_{h_i}\}_{i=0}^\ell$ of simplicial triangulations and corresponding finite element spaces $\mathbf{V}_{h_i}, W_{h_i}$, $0 \leq i \leq \ell$. Alternatively, we have used BPX preconditioned CG applied to the Schur complement system associated with (3.6), observing that $\tilde{S} = \tilde{A}^{-1}S$ is the Schur complement matrix of the preconditioned saddle point problem. For a systematic comparison of the performance of these multilevel preconditioned iterative solvers, we refer to [20].

We have performed numerical simulations of SAWs for plates of length L , width W , and height H such that $\Omega_1 := (0, L) \times (0, W) \times (0, H)$ with $\Gamma_{p,D} := [0, L] \times [0, W] \times \{0\}$. As the piezoelectric material we have assumed Lithiumniobate ($LiNbO_3$). Table 3.1 contains the elasticity tensor \mathbf{c} , the piezoelectric tensor $\boldsymbol{\varepsilon}$, the electric permittivity tensor $\boldsymbol{\epsilon}$, and the density ρ_p of this material.

Table 3.1: Piezoelectric material moduli (Lithiumniobate $LiNbO_3$)

Elast. tensor $10^{10} \frac{N}{m^2}$	$c_{11} = c_{22}$ 20.3	c_{12} 5.3	$c_{13} = c_{23}$ 7.5	$c_{14} = -c_{24} = c_{56}$ 0.9	c_{33} 24.5	$c_{44} = c_{55}$ 6.0	c_{66} 7.5
Piezoel. tensor $\frac{C}{m^2}$	$e_{15} = e_{24}$ 3.7		$e_{22} = -e_{21} = -e_{16}$ 2.5		$e_{31} = e_{32}$ 0.1		e_{33} 1.3
Permitt. tensor $10^{-12} \frac{F}{m}$	$\epsilon_{11} = \epsilon_{22}$ 749.0		ϵ_{33} 253.2	Density $10^3 \frac{kg}{m^3}$		ρ_p 4.63	

The IDT has been positioned at the top of the plate, i.e., $\Gamma_{E,D} := [L_1, L_2] \times [W_1, W_2] \times \{L\}$, and has been assumed to operate at a frequency $\omega/(2\pi) = 100 \text{ MHz}$ thus generating SAWs of wavelength $\lambda = 40 \mu m$. In order to control the finite element error appropriately, following [34] we have chosen an initial mesh of mesh length $h \lesssim \sqrt{\lambda^3}$.

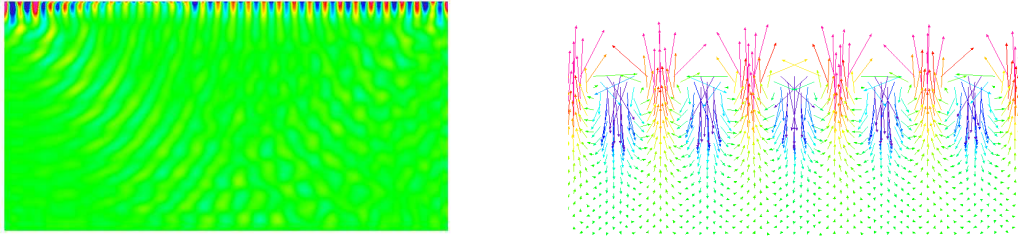


Fig. 3.1. Amplitudes of an electric potential wave (left) and elliptic displacement (right)

For a plate of length $L = 1.2 \text{ mm}$, width $W = 0.6 \text{ mm}$, height $H = 0.6 \text{ mm}$, and $\Gamma_{E,D} := [0.2, 0.4] \times [0.1, 0.5] \times \{1.2\}$, Fig. 3.1 (left) shows the computed amplitudes of the electric potential wave for the longitudinal section $[0, 1.2] \times \{0.3\} \times [0, 0.6]$.

As can be clearly seen, the SAWs are strictly confined to the surface of the piezoelectric material with a penetration depth of approximately one wavelength. The SAW velocity is $4.0 \cdot 10^3 \text{ m/s}$. Fig. 3.1 (right) displays the typical elliptic displacement of Rayleigh waves, i.e., the amplitudes of the surface displacement in the x_1 - and x_3 -direction are 90° out of phase.

For the simulation of the SAW induced fluid flow in the microchannels of the biochip, we have numerically solved the two systems (2.16a)-(2.16c) and (2.18a)-(2.18c) obtained from the compressible Navier-Stokes equations (2.12a)-(2.12d) by the homogenization approach as described in subsection 2.2.

For discretization in space, we have used Taylor-Hood P2-P1 elements with respect to a geometrically conforming simplicial triangulation $\mathcal{T}_h(\Omega_2)$ of the computational domain Ω_2 occupied by the fluid, i.e., we have chosen the finite element spaces

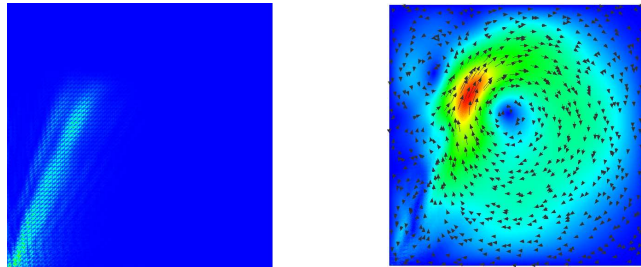


Fig. 3.2. Effective force (left) and associated vortex (right)

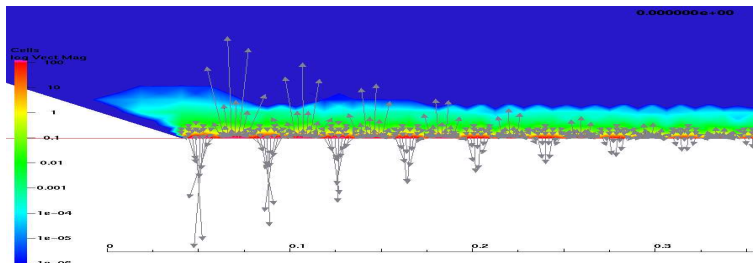


Fig. 3.3. Propagation and damping of SAWs in a microchannel

$$\mathbf{V}_h := \left\{ \mathbf{v}_h \in C(\Omega_2)^3 \mid \mathbf{v}_h|_T \in P_2(T)^3, T \in \mathcal{T}_h(\Omega_2) \right\},$$

$$W_h := \left\{ w_h \in C(\Omega_2) \mid w_h|_T \in P_1(T), T \in \mathcal{T}_h(\Omega_2) \right\},$$

and $\mathbf{V}_{\mathbf{g}_{h,i}} := \mathbf{V}_h \cap \mathbf{V}_{\mathbf{g}_{h,i}}$ with $\mathbf{g}_{h,i}$ being a piecewise quadratic approximation of $\mathbf{g}_i, 1 \leq i \leq 2$ (cf., e.g., [22]). The boundary data have been chosen according to the computation of the displacements \mathbf{u}_h obtained by the numerical solution of the piezoelectric equations as described in subsection 3.1. For discretization in time of (2.16a)-(2.16c), we have used the Θ -scheme with respect to a uniform partitioning of the time interval of step size k and a preferred choice of $\Theta = 1$ (backward Euler scheme) or $\Theta = 1/2$ (Crank-Nicolson). The chosen discretizations amount to the numerical solution of algebraic saddle point problems of the form

3.2. Simulation of acoustic streaming

$$\begin{pmatrix} A & B \\ B^T & 0 \end{pmatrix} \begin{pmatrix} v \\ p \end{pmatrix} = \begin{pmatrix} b_1 \\ b_2 \end{pmatrix},$$

which has been done using a multilevel preconditioned inexact Uzawa algorithm [13] with respect to a hierarchy $\{\mathcal{T}_{h_i}\}_{i=0}^\ell$ of triangulations.

Table 3.2: Microfluidic material data (water at 20°)

ρ_f	η	ξ	c_0
$1.0 \cdot 10^3 \text{ kg/m}^3$	$1.002 \cdot 10^{-4} \text{ kg/(ms)}$	$7.97 \cdot 10^{-4} \text{ kg/(ms)}$	$1.484 \cdot 10^3 \text{ m/s}$

The fluid in the microchannels has been assumed to be water with the relevant constants ρ_f, η , and ξ as well as the small sound velocity c_0 listed in Table 3.2.

For the simulation of the penetration of the SAWs into a microchannel and the creation of sharp jets we have chosen $\Omega_2 := (0, L) \times (0, W) \times (0, H)$ and $\Gamma_{2,D} := [0, L_1] \times [0, W] \times \{0\}$ assuming a maximal displacement of the lower wall of $\varepsilon = 1.0 \cdot 10^{-9} \text{ m}$.

For $L = W = H = 2.5 \cdot 10^2 \mu\text{m}$ and $L_1 = 0.25 \cdot 10^2 \mu\text{m}$, Fig. 3.2 (left) shows the effective force which is the time-averaged sound velocity in the fluid, whereas Fig. 3.2 (right) displays the associated velocity field, both at the longitudinal section $[0, L] \times \{1.25\} \times [0, H]$.

Fig. 3.3 illustrates the computed propagation of the SAWs in a microchannel where the SAWs penetrate the channel at its lower left end. The SAWs propagate from the left to the right and experience a significant damping.

4. Shape optimization

We have performed shape optimizations of the walls of the microchannels and reservoirs using objective functionals of tracking type or representing the pumping rate at selected cross sections with the systems (2.16) and (2.18a)-(2.18c) as the underlying state equations.

The optimal design of the shape or topology of structures is an area within the theory of optimization with applications, e.g., in aero- and fluid dynamics, electromagnetics, and mechanics whose importance is reflected by a series of monographs on this topic that have been published during the past decades (cf. [1, 7, 8, 11, 24, 27, 28, 38, 42, 45]).

A typical shape optimization problem associated with a time-independent PDE or a system thereof as the underlying state equation amounts to the minimization of a shape functional J over bounded domains Ω in Euclidean space \mathbb{R}^d . The state function u is assumed to satisfy a boundary value problem as described by means of a partial differential operator L , and there may be further equality and/or inequality constraints on the domain.

$$\inf_{\Omega} J(u, \Omega), \quad J(u, \Omega) := \int_{\Omega} j(x, u(x)) \, dx, \quad (4.1a)$$

$$\text{subject to } L_{\Omega}u = f_{\Omega} \quad \text{in } \Omega, \quad u = g_{\Omega} \quad \text{on } \Gamma, \quad h(\Omega) \geq 0. \quad (4.1b)$$

In order to cope with the inherent difficulty that the minimization is over a certain class of domains instead of a set of functions in an appropriate function space, we have used the classical approach based on a parametrization of the domain by a finite number of design variables: the boundary Γ is represented by a composite Bézier curve using a certain number of Bézier control points $d \in \mathbb{R}^m$, $m \in \mathbb{N}$, which serve as design variables. The equality and/or inequality constraints are expressed by means of the design variables. For the finite element approximation of (4.1) we choose \hat{d} as reference design variable and refer to $\hat{\Omega} := \Omega(\hat{d})$ as the associated reference domain. Then, the actual domain $\Omega(d)$ can be obtained from the reference domain $\hat{\Omega}$ by means of a mapping $\Omega(d) = \Phi(\hat{\Omega}; d)$. The advantage of using the reference domain $\hat{\Omega}$ is that finite element approximations can be performed with respect to that fixed domain without being forced to remesh for every new set of the design variables.

An alternative approach would be the use of shape calculus [11], i.e., of shape gradients and shape Hessians in case of interior-point methods requiring first and second order information. Since stable numerical implementations of shape Hessians were not available at the time the research has been conducted, we decided to use the standard approach described above.

The finite element discretization of (4.1) with respect to a simplicial triangulation $\mathcal{T}_h(\Omega)$ of the computational domain Ω leads to a finite dimensional optimization problem

$$\inf_{u_h, d} J_h(u_h, d), \quad (4.2a)$$

$$\text{subject to } L_h u_h = b_h, \quad h_j(d) \geq 0, \quad 1 \leq j \leq s, \quad (4.2b)$$

where $u_h \in \mathbb{R}^n$ is the finite element approximation of the state u , $J_h(u_h, d)$ the discretized objective functional and $L_h u_h = b_h$ the algebraic system arising from the finite element discretization of the PDE.

The inequality constrained optimization problem (4.2) represents a large-scale nonlinear programming problem. For such problems, efficient numerical solution techniques have been developed. Interior point methods belong to the methods of choice. In particular, we have used adaptive multilevel path-following interior point methods. For ease of notation, in the sequel we will drop the subindex h . The inequality constraints in (4.2b) are coupled by logarithmic barrier functions with a barrier parameter $\beta = 1/\mu > 0$, $\mu \rightarrow \infty$, and the equality constraint by a Lagrange multiplier $\lambda \in \mathbb{R}^n$. This leads to the saddle point problem

$$\inf_{u, d} \sup_{\lambda} \mathcal{L}^{(\mu)}(u, \lambda, d), \quad (4.3)$$

where $\mathcal{L}^{(\mu)}$ stands for the Lagrangian

$$\mathcal{L}^{(\mu)}(u, \lambda, d) = B^{(\mu)}(u, d) + \langle \lambda, Lu - b \rangle. \quad (4.4)$$

Here, $B^{(\mu)}(u, d)$ is the barrier function as given by

$$B^{(\mu)}(u, d) := J(u, d) - \frac{1}{\mu} \sum_{j=1}^s \ln(h_j(d)). \quad (4.5)$$

and $\langle \cdot, \cdot \rangle$ stands for the Euclidean inner product on \mathbb{R}^n . The barrier path $\mu \mapsto x(\mu) := (u(\mu), \lambda(\mu), d(\mu))^T$ is given as the solution of the nonlinear system

$$F(x(\mu), \mu) = \begin{pmatrix} \mathcal{L}_u^{(\mu)}(u, \lambda, d) \\ \mathcal{L}_\lambda^{(\mu)}(u, \lambda, d) \\ \mathcal{L}_d^{(\mu)}(u, \lambda, d) \end{pmatrix} = 0, \quad (4.6)$$

where the subindices refer to the derivatives of the Lagrangian with respect to the primal, the dual, and the design variables. The choice of the barrier parameter strongly influences the performance of the interior point method. There are static strategies with the Fiacco-McCormick approach as the most prominent one (cf. [18]), where the barrier parameter is fixed until an approximate solution has been obtained, and there is a variety of dynamic update strategies (cf. [6, 16, 21, 40, 47–49]). Convergence properties of the Fiacco-McCormick approach have been studied in [10] and [50], whereas a convergence analysis of dynamic update strategies has been addressed in [6, 16, 40, 48]. We have considered the solution of (4.6) by an adaptive continuation method based on the affine invariant convergence theory of Newton-type methods (see, e.g., [12]).

The adaptive continuation method is a predictor-corrector method with an adaptively determined continuation step size in the predictor and Newton's method as a corrector. It relies on the affine invariant convergence theory of Newton and Newton-type methods and ensures that the iterates stay within a neighborhood ('contraction tube') of the barrier path so that convergence to a local minimum of the original minimization problem can be achieved (cf. Fig. 4.1).

Predictor Step: The predictor step relies on tangent continuation along the trajectory of the Davidenko equation

$$F_x(x(\mu), \mu) x'(\mu) = -F_\mu(x(\mu), \mu) \quad (4.7)$$

and amounts to the implementation of an explicit Euler step: Given some approximation $\tilde{x}(\mu_k)$ at $\mu_k > 0$, compute $\tilde{x}^{(j_0)}(\mu_{k+1})$, where $\mu_{k+1} = \mu_k + \Delta\mu_k^{(j)}$, according to

$$F_x(\tilde{x}(\mu_k), \mu_k) \delta x(\mu_k) = -F_\mu(\tilde{x}(\mu_k), \mu_k), \quad (4.8a)$$

$$\tilde{x}^{(j_0)}(\mu_{k+1}) = \tilde{x}(\mu_k) + \Delta\mu_k^{(j)} \delta x(\mu_k), \quad (4.8b)$$

starting with $j = 0$ ($j \geq 1$ only if required by the correction step (see below)). We use $\Delta\mu_0^{(0)} = \Delta\mu_0$ for some given initial step size $\Delta\mu_0$, whereas for $k \geq 1$ the predicted step size $\Delta\mu_k^{(0)}$ is chosen by

$$\Delta\mu_k^{(0)} := \left(\frac{\|\Delta x^{(j_0)}(\mu_k)\|}{\|\tilde{x}(\mu_k) - \tilde{x}^{(j_0)}(\mu_k)\|} \frac{\sqrt{2} - 1}{2\Theta(\mu_k)} \right)^{1/2} \Delta\mu_{k-1}, \quad (4.9)$$

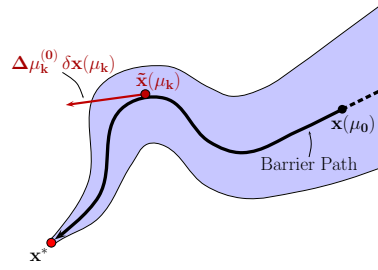


Fig. 4.1. Predictor step of the adaptive continuation method.

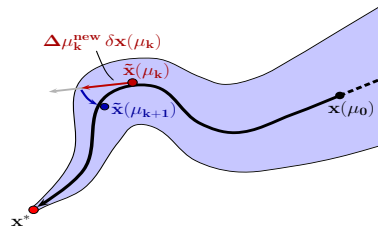


Fig. 4.2. Correction step of the adaptive continuation method.

where $\Delta\mu_{k-1}$ is the computed continuation step size, $\Delta x^{(j_0)}(\mu_k)$ is the first Newton correction (see below), and $\Theta(\mu_k) < 1$ is the contraction factor associated with a successful previous continuation step.

Corrector step: As a corrector, we use Newton's method applied to $F(x(\mu_{k+1}), \mu_{k+1}) = 0$ with $\tilde{x}^{(j_0)}(\mu_{k+1})$ from (4.8b) as a start vector. In particular, for $\ell \geq 0$ (Newton iteration index) and $j_\ell \geq 0$ (j being the steplength correction index) we compute $\Delta x^{(j_\ell)}(\mu_{k+1})$ according to

$$F_x(\tilde{x}^{(j_\ell)}(\mu_{k+1}), \mu_{k+1}) \Delta x^{(j_\ell)}(\mu_{k+1}) = -F(\tilde{x}^{(j_\ell)}(\mu_{k+1}), \mu_{k+1}), \quad (4.10)$$

update $\tilde{x}^{(j_{\ell+1})}(\mu_{k+1}) := \tilde{x}^{(j_\ell)}(\mu_{k+1}) + \Delta x^{(j_\ell)}(\mu_{k+1})$ and compute $\overline{\Delta x}^{(j_\ell)}(\mu_{k+1})$ as the associated simplified Newton correction

$$F_x(\tilde{x}^{(j_\ell)}(\mu_{k+1}), \mu_{k+1}) \overline{\Delta x}^{(j_\ell)}(\mu_{k+1}) = -F(\tilde{x}^{(j_\ell)}(\mu_{k+1}) + \Delta x^{(j_\ell)}(\mu_{k+1}), \mu_{k+1}).$$

The convergence of Newton's method is monitored by means of

$$\Theta^{(j_\ell)}(\mu_{k+1}) := \|\overline{\Delta x}^{(j_\ell)}(\mu_{k+1})\| / \|\Delta x^{(j_\ell)}(\mu_{k+1})\|.$$

In case of successful convergence, we set $\tilde{x}(\mu_{k+1}) := \tilde{x}^{(j_\ell)}(\mu_{k+1})$ with ℓ being the current Newton iteration index, accept the current step size $\Delta\mu_k := \Delta\mu_k^{(j)}$ with current steplength correction index j and proceed with the next continuation step. However, if the monotonicity test

$$\Theta^{(j_\ell)}(\mu_{k+1}) < 1 \quad (4.11)$$

fails for some $j_\ell \geq 0$, the predicted steplength $\Delta\mu_k^{(j)}$ has been chosen too large so that the predicted solution $\tilde{x}^{(j_0)}(\mu_{k+1})$ is not situated within the Kantorovich neighborhood of $x(\mu_{k+1})$, i.e., it is outside the contraction tube around the barrier path (cf. Fig. 4.2). The corrector

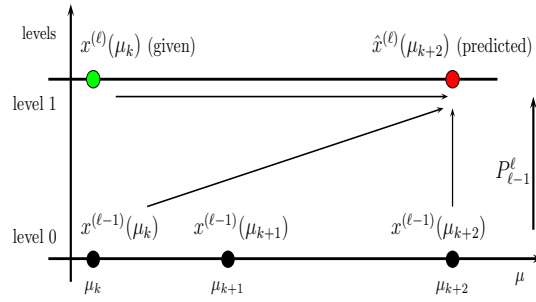


Fig. 4.3. Two-level predictor-corrector scheme

step provides a correction of the steplength for the tangent direction $\delta x(\mu_k)$ such that the new iterate stays within the contraction tube. To do so, the continuation step from (4.8b) has to be repeated with the reduced step size

$$\Delta\mu_k^{(j+1)} := \left(\frac{\sqrt{2} - 1}{g(\Theta^{(j\ell)})} \right)^{1/2} \Delta\mu_k^{(j)}, \tag{4.12}$$

$$g(\Theta) := \sqrt{\Theta + 1} - 1$$

until we either achieve convergence or for some prespecified lower bound $\Delta\mu_{min}$ observe

$$\Delta\mu_k^{(j+1)} < \Delta\mu_{min} .$$

In the latter case, we stop the algorithm and report convergence failure.

The Newton steps are realized by an inexact Newton method featuring right-transforming iterations (cf., e.g., [30, 32, 33, 36, 52]). The derivatives occurring in the KKT conditions and the Hessians are computed by automatic differentiation (cf., e.g., [23]).

The predictor-corrector scheme is performed in a multilevel framework with respect to a hierarchy of discretizations following the ideas developed for parameter dependent nonlinear elliptic problems in [26, 31]. We describe the multilevel approach in case of a two-level scheme with the levels $\ell - 1$ and ℓ (cf. Fig. 4.3). The prediction is done by nested iteration in such a way that a certain number of adaptive continuation steps are performed on the coarser level $\ell - 1$ before a predicted value is computed on the finer level ℓ . The corrector is a Newton multigrid method incorporating a two-level PDE solver featuring appropriate smoothers. The iterates are checked for acceptance by the level ℓ monotonicity test. In some more detail, we illustrate the two-level scheme in case of two continuation steps on level $\ell - 1$. We assume that

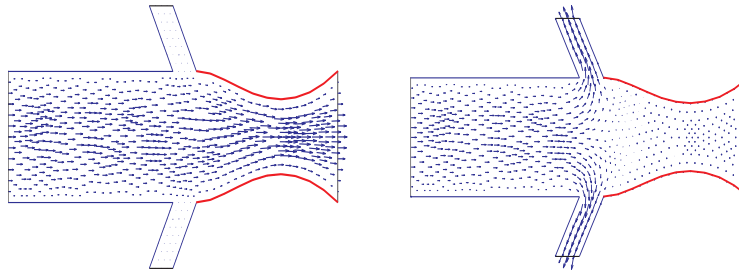


Fig. 4.4. Capillary barrier: Velocity profile in the flow mode (left) and in the stopping mode (right)

approximations $x^{\ell-1}(\mu_k)$ and $x^\ell(\mu_k)$ are available for some continuation parameter μ_k . Firstly, we perform two continuation steps with an adaptive choice of the continuation steplengths. Secondly, we use the level $\ell - 1$ approximations $x^{\ell-1}(\mu_k)$ and $x^{\ell-1}(\mu_{k+2})$ as well as the level ℓ approximation $x^\ell(\mu_k)$ to obtain a level ℓ prediction at μ_{k+2} . This approximation is then corrected by the two-level Newton multigrid scheme and checked for acceptance by the level ℓ monotonicity test. In the general case of more than two levels, the multilevel predictor-corrector continuation method consists of a recursive application of the two-level scheme.

For a detailed documentation of numerical results including a comparison with dynamic update strategies, we refer to [3–5, 29].

We have used the adaptive multilevel barrier method for the optimal design of a pressure driven capillary barrier between a channel and a reservoir (cf. Fig. 1.2) where the objective functional has been chosen of tracking type

$$J(\mathbf{v}_2, p_2, d) := \frac{1}{2} \|\mathbf{v}_2 - \mathbf{v}_2^*\|_{0, \Omega_2(d)}^2 + \frac{1}{2} \|p_2 - p_2^*\|_{0, \Omega_2(d)}^2 \quad (4.13)$$

with desired velocity and pressure profiles \mathbf{v}_2^*, p_2^* provided by our industrial cooperation partner [41]. The state equation for (\mathbf{v}_2, p_s) is the compressible Stokes system (2.18a)-(2.18c). As computational domain we have chosen part of a channel with a capillary barrier at its end and part of a reservoir connected with the channel by the capillary barrier. The channel additionally has passive outlet valves (cf. Fig.4.4) that are activated when the barrier operates in stopping mode and back flow occurs. The stopping behavior has been modeled by Signorini type boundary conditions between the channel and the reservoir with respect to a pressure threshold. We have further chosen a total of 12 Bézier control points $d_j, 1 \leq j \leq 12$, for the representation of the upper and lower boundary of the capillary barrier as a composite Bézier curve such that $d_j^{(min)} \leq d_j \leq d_j^{(max)}, 1 \leq j \leq 12$, with bounds $d_j^{(min)}, d_j^{(max)}$ derived from technological constraints provided by [41].

Table 4.1: History of the adaptive multilevel predictor-corrector strategy (3 Levels)

<i>level</i>	<i>k</i>	μ	$\Delta\mu$	ΔJ	<i>CPU</i>
1	1	2.0E+02			
	2	6.4E+02	4.4E+02	2.99E-05	
	3	9.9E+02	3.5E+02	3.40E-06	
	4	1.4E+03	4.1E+02	1.25E-06	
	5	2.0E+03	6.0E+02	9.30E-08	
2	3	9.9E+02	7.9E+02		
	5	2.0E+03	1.8E+03		
3	5	2.0E+03	1.8E+03		4h 30m

Fig. 4.4 shows the computed optimal shape of the barrier and the associated velocity fields when the barrier is in the flow mode (left) and in the stopping mode (right).

In case of three levels, the history of the adaptive multilevel barrier method is illustrated in Table 4.1, where μ stands for the inverse of the barrier parameter, $\Delta\mu$ for the increase in μ , and ΔJ for the decrease in the objective functional (the constraints were not active at optimality so that the value of J at optimality was zero). For a comparison, the results of a multilevel version of Mehrotra’s predictor-corrector scheme are displayed in Table 4.2 with σ denoting the centering parameter (cf. [4]). The computations have been performed on a machine with a 2.66

Table 4.2: History of a multilevel version of Mehrotra's predictor-corrector scheme (3 Levels)

<i>level</i>	<i>k</i>	μ	σ	ΔJ	<i>CPU</i>
1	1	2.0E+02	1.2E-05		
	2	3.2E+03	8.7E-02	4.65E-01	
	3	1.1E+03	1.2E-05	6.79E-04	
	4	7.2E+03	7.1E-07	1.80E-05	
	5	4.9E+04	1.2E-09	1.18E-06	
2	3	1.1E+03	1.2E-05		
	5	4.9E+04	1.2E-09		
3	5	4.9E+04	1.2E-09		5h 40m

GHz Intel(R) Core(TM)2 Duo processor running Linux Fedora 8. For further results we refer to [4, 5].

Acknowledgments. The authors are thankful to anonymous referees for valuable suggestions that led to an improvement of the manuscript. They further acknowledge support by the NSF under Grants No. DMS-0511611, DMS-0707602, DMS-0810156, DMS-0811153, and by the German National Science Foundation DFG within the Priority Program SPP 1253.

References

- [1] G. Allaire, *Shape Optimization by the Homogenization Method*, Springer, Berlin-Heidelberg-New York, 2002.
- [2] H. Antil, A. Gantner, R.H.W. Hoppe, D. Köster, K.G. Siebert, and A. Wixforth, *Modeling and simulation of piezoelectrically agitated acoustic streaming on microfluidic biochips*, in *Proc. 17th Int. Conf. on Domain Decomposition Methods (Langer, U. et al.; eds.), Lecture Notes in Computational Science and Engineering, Vol. 60*, pp. 305–312, Springer, Berlin Heidelberg-New York, 2007.
- [3] H. Antil, R.H.W. Hoppe, and C. Linsenmann, *Path-following primal-dual interior-point methods for shape optimization of stationary flow problems*, *J. Numer. Math.*, **11** (2007), 81-100.
- [4] H. Antil, R.H.W. Hoppe, and C. Linsenmann, *Optimal design of stationary flow problems by path-following interior-point methods*, *Control & Cybernetics*, **37**, 771–796, 2008.
- [5] H. Antil, R.H.W. Hoppe, and C. Linsenmann, *Adaptive multilevel interior-point methods in PDE constrained optimization*, *Proc. 18th Int. Conf. on Domain Decomposition Methods and Applications (Bercovier, M. et al.; eds.), Lecture Notes in Computational Science and Engineering*, Springer, Berlin Heidelberg-New York, 2009 (in press).
- [6] P. Armand, J. Benoist, and D. Orban, *Dynamic updates of the barrier parameter in primal-dual methods for nonlinear programming*, *Computational Optimization and Applications*, **41** (2008), 1-25.
- [7] M.P. Bendsøe, *Optimization of Structural Topology, Shape, and Material*, Springer, Berlin-Heidelberg-New York, 1995.
- [8] M.P. Bendsøe and O. Sigmund, *Topology Optimization: Theory, Methods and Applications*, Springer, Berlin-Heidelberg-New York, 2003.
- [9] F. Brezzi and M. Fortin, *Mixed and Hybrid Finite Element Methods*, Springer, Berlin-Heidelberg-New York, 1991.
- [10] R.H. Byrd, J.C. Gilbert, and J. Nocedal, *A trust region method based on interior point techniques for nonlinear programming*, *Math. Programming*, **89** (2000), 149-185.
- [11] M.C. Delfour and J.P. Zolesio, *Shapes and Geometries: Analysis, Differential Calculus and Optimization*, SIAM, Philadelphia, 2001.

- [12] P. Deuffhard, *Newton Methods for Nonlinear Problems. Affine Invariance and Adaptive Algorithms*, Springer, Berlin-Heidelberg-New York, 2004.
- [13] H.C. Elman, *Preconditioners for saddle point problems arising in computational fluid dynamics*, Appl. Numer. Math. **43** (2002), 75-89.
- [14] W. E and B. Enquist, *The heterogeneous multiscale methods*, Comm. Math. Sciences, **1** (2003), 87-132, 2003.
- [15] W. E and B. Enquist, *The heterogeneous multiscale method for homogenization problems*, in *Multiscale Methods in Sci. and Engrg.*, pp. 89-110, Lect. Notes in Comput. Sci. Engrg., Vol. 44, Springer, Berlin-Heidelberg-New York, 2005.
- [16] A.S. El-Bakry, R.A. Tapia, T. Tsuchiya, and Y. Zhang, *On the formulation and theory of the Newton interior-point method for nonlinear programming*, Journal of Optimization Theory and Applications, **89** (1996), 507-541.
- [17] A.C. Eringen and G.A. Maugin, *Electrodynamics of Continua I. Foundations and Solid Media*, Springer, Berlin-Heidelberg-New York, 1990.
- [18] A.V. Fiacco and G.P. McCormick, *Nonlinear Programming: Sequential Unconstrained Minimization Techniques*, SIAM, Philadelphia, 1990.
- [19] T. Franke and A. Wixforth, *Microfluidics for miniaturized laboratories on a chip*, ChemPhysChem, **9** (2008), 2140-2156. 2008.
- [20] A. Gantner, R.H.W. Hoppe, D. Köster, K.G. Siebert, and A. Wixforth, *Numerical simulation of piezoelectrically agitated surface acoustic waves on microfluidic biochips*, Comp. Visual. Sci., **10** (2007), 145-161.
- [21] D.M. Gay, M.I. Overton, and M.H. Wright, *Primal-dual interior method for nonconvex nonlinear programming*, in *Advances in Nonlinear Programming*(Y. Yuan; ed.), pp. 31-56, Kluwer, Dordrecht, 1998.
- [22] R. Glowinski, *Handbook of Numerical Analysis: Numerical Methods for Fluids*, Elsevier, Amsterdam, 2004.
- [23] A. Griewank, *Evaluating Derivatives, Principles and Techniques of Automatic Differentiation*, SIAM, Philadelphia, 2000.
- [24] M.D. Gunzburger, *Perspectives in Flow Control and Optimization*, SIAM, Philadelphia, 2003.
- [25] Z. Guttenberg, H. Müller, H. Habermüller, A. Geisbauer, J. Pipper, J. Felbel, M. Kilepinski, J. Scriba, and A. Wixforth, *Planar chip device for PCR and hybridization with surface acoustic wave pump*, Lab Chip **5** (2005), 308-317.
- [26] W. Hackbusch, *Multi-grid continuation methods*, in *Iterative Solution of Nonlinear Systems* (R. Ansorge et al.; eds.), pp. 20-45, Springer, Berlin-Heidelberg-New York, 1982.
- [27] J. Haslinger and R.A.E. Mäkinen, *Introduction to Shape Optimization: Theory, Approximation, and Computation*, SIAM, Philadelphia, 2004.
- [28] J. Haslinger and P. Neittaanmäki, *Finite Element Approximation for Optimal Shape Design: Theory and Applications*, John Wiley & Sons, Chichester, 1988.
- [29] R.H.W. Hoppe, C. Linsenmann, and H. Antil, *Adaptive path following primal dual interior point methods for shape optimization of linear and nonlinear Stokes flow problems*, in *Lecture Notes in Computer Science, Vol. 4818*, Springer, Berlin-Heidelberg-New York, 2008, pp. 259-266.
- [30] R.H.W. Hoppe, C. Linsenmann, and S.I. Petrova, *Primal-dual Newton methods in structural optimization*, Comp. Visual. Sci., **9** (2006), 71-87.
- [31] R.H.W. Hoppe and H.D. Mittelmann, *A multi-grid continuation strategy for parameter dependent variational inequalities*, J. Comput. Appl. Math. **26** (1989), 35-46.
- [32] R.H.W. Hoppe and S.I. Petrova, *Primal-dual Newton interior-point methods in shape and topology optimization*, Numer. Linear Algebra Appl., **11** (2004), 413-429.
- [33] R.H.W. Hoppe, S.I. Petrova, and V. Schulz, *A primal-dual Newton-type interior-point method for topology optimization*, Journal of Optimization: Theory and Applications, **114**, (2002), 545-571.
- [34] F. Ihlenburg, *Finite Element Analysis of Acoustic Scattering*, Springer, Berlin-Heidelberg-New

- York, 1998.
- [35] D. Köster, *Numerical simulation of acoustic streaming on SAW-driven biochips*, SIAM J. Sci. Comput., **29** (2007), 2352-2380.
 - [36] B. Maar and V. Schulz, *Interior point methods in topology optimization*, Structural Optimization, **19** (2000), 214-224.
 - [37] G.A. Maugin, *Continuum Mechanics of Electromagnetic Solids*, North-Holland, Amsterdam, 1987.
 - [38] B. Mohammadi and O. Pironneau, *Applied Shape Optimization for Fluids*, Oxford University Press, Oxford, 2001.
 - [39] J. Nocedal and M. Overton, *Projected Hessian updating algorithms for nonlinearly constrained optimization*, SIAM J. Numer. Anal., **22** (1985), 821-850.
 - [40] J. Nocedal, A. Wächter, and R.A. Waltz, *Adaptive barrier update strategies for nonlinear interior methods*, Research Report RC 23563, IBM T. J. Watson Research Center, Yorktown, 2006.
 - [41] Olympus Medical Systems, *private communication*, 2008.
 - [42] O. Pironneau, *Optimal Shape Design for Elliptic Systems*, Springer, Berlin-Heidelberg-New York, 1984.
 - [43] J. Pollard and B. Castrodale, *Outlook for DNA microarrays: emerging applications and insights on optimizing microarray studies*, Report. Cambridge Health Institute, Cambridge 2003.
 - [44] M. Renardy and R.C. Rogers, *An Introduction to Partial Differential Equations*, Springer, Berlin-Heidelberg-New York, 1993.
 - [45] J. Sokolowski and J.P. Zolesio, *Introduction to Shape Optimization*, Springer, Berlin-Heidelberg-New York, 1992.
 - [46] T.M. Squires and S.R. Quake, *Microfluidics: fluid physics at the nanoliter scale*, Rev. Mod. Phys., **77** (2005), 977-1026.
 - [47] A.L. Tits, A. Wächter, S. Bakhtiari, T.J. Urban, and C.T. Lawrence, *A primal-dual interior-point method for nonlinear programming with strong global and local convergence properties*, SIAM J. on Optimization, **14** (2003), 173-199.
 - [48] M. Ulbrich, S. Ulbrich, and L. Vicente, *A globally convergent primal-dual interior point filter method for nonconvex nonlinear programming*, Math. Programming, **100** (2004), 379-410.
 - [49] R.J. Vanderbei and D.F. Shanno, *An interior point algorithm for nonconvex nonlinear programming*, Computational Optimization and Applications, **13** (1999), 231-252.
 - [50] A. Wächter and L.T. Biegler, *Line search filter methods for nonlinear programming: motivation and global convergence*, SIAM J. on Optimization, **16** (2005), 1-31.
 - [51] G.M. Whitesides, *The origins and the future of microfluidics*, Nature, **44** (2006), 368.
 - [52] G. Wittum, *On the convergence of multigrid iterations with transforming smoothers. Theory with applications to the Navier-Stokes equations*, Numer. Math., **57** (1989), 15-38.
 - [53] A. Wixforth, *Acoustically driven programmable microfluidics for biological and chemical applications*, JALA, **11** (2006), 399-405.
 - [54] A. Wixforth, C. Strobl, C. Gauer, A. Toegl, J. Scriba, and Z. Guttenberg, *Acoustic manipulation of small droplets*, Anal. Bioanal. Chem., **379** (2004), 982-991.
 - [55] E. Zeidler, *Nonlinear Functional Analysis and Its Applications. II/A: Linear Monotone Operators*, Springer, Berlin-Heidelberg-New York, 1990.